Problem Solutions

CHAPTER 1

1.1. As we have discussed, a Fluids-DFT is typically formulated in an open ensemble in which the state variables are the temperature *T*, volume *V*, and chemical potentials of all the species, μ_α. Thus for a single-component membrane system consisting of lipids and solvent, we must specify four variables: μ_s, μ_L, *V*, and *T*. In the CMS-DFT, the chemical potentials are determined by the densities in the bulk reservoir. One way to set these is to fix the total bulk site density $\rho_b = \rho_L + \rho_s$ and then to consider bilayer properties as a function of the solvent number fraction $x_s = \rho_s / \rho_b$. Note that at fixed *T, V*, and ρ_b, the additional constraint of $\gamma = 0$ uniquely determines x_s, so that there is only one bilayer for this set of conditions. We identify this unique bilayer solution as the physical one for a bilayer at that particular temperature (this assumes our choice of the overall density is a realistic one, i.e., resulting in realistic overall fluid densities).

What happens if we now add a second component to the bilayer, such as the alcohols discussed in the text? We now have three chemical potentials: μ_s, μ_L, and μ_a for the alcohol. We still need to maintain the constraint $\gamma = 0$. What is the dimensionality of the set of possible membrane solutions at zero tension and fixed temperature and volume? How might we choose the chemical potential variables to obtain physically realistic results?

Answer

We now have five variables that describe the thermodynamic state of the system. At fixed *T, V,* and $\gamma = 0$, we have three constraints, so the set of possible bilayers under these conditions forms a two-dimensional surface in phase space, which could be parameterized by any two of the three chemical potentials (or any two combinations of these). If we follow our previous work and again keep ρ_b fixed, we now have a one-dimensional "line" of possible bilayers. There are various possible ways one could set, e.g., x_s and $x_a = \rho_a / \rho_b$ to choose a specific bilayer from this line. For a discussion, see the appendix in [16].

1.2. Consider the CMS-DFT described in the text (§1.3.1). The free energy is given by a functional Taylor expansion about the bulk reference state up to second order in the density as expressed in Eq. (10). Explain why this implies that the CMS-DFT cannot support a fluid/vapor phase transition or interface.

Answer

A fluid/vapor phase transition occurs in a single-component fluid. From Eq. (1.18), the grand free energy for a bulk density $\rho(r) \equiv \rho$ (different than the reference density) is given by

$$\Delta\Omega = -\frac{V}{N}\left(\rho - \rho_r\right) + \frac{1}{2}\int drc_{\alpha\beta}(r)\left[\rho^2 - \rho_r^2\right],$$

The free energy is thus quadratic in r. A quadratic function cannot have two minima, which is required for liquid/vapor coexistence (two minima in the free energy, one corresponding to the bulk liquid phase and the other to the bulk vapor phase). Thus, the CMS-DFT cannot describe, e.g., free liquid interfaces or wetting phenomena where there is a vapor phase. Also see the explanation beginning on p. 103 in Evans R. 1992. Density functionals in the theory of nonuniform fluids. In *Fundamentals of inhomogeneous fluids*. Ed D Henderson. New York: Marcel Dekker.

CHAPTER 2

2.1. Prove Ricci's lemma, namely, that both $\nabla_a g_{bc} = 0$ and $\nabla_a g = 0$.

Answer

Using the definition of the covariant derivative and the Christoffel symbols, we get

$$\begin{aligned}
\nabla_a g_{bc} &= \partial_a g_{bc} - \Gamma^d_{ab} g_{dc} - \Gamma^d_{ac} g_{bd} \\
&= \partial_a g_{bc} - \tfrac{1}{2} g^{de}\left(\partial_a g_{be} + \partial_b g_{ea} - \partial_e g_{ab}\right) g_{dc} - \tfrac{1}{2} g^{de}\left(\partial_a g_{ce} + \partial_c g_{ea} - \partial_e g_{ac}\right) g_{bd} \\
&= \partial_a g_{bc} - \tfrac{1}{2}\delta^e_c\left(\partial_a g_{be} + \partial_b g_{ea} - \partial_e g_{ab}\right) - \tfrac{1}{2}\delta^e_b\left(\partial_a g_{ce} + \partial_c g_{ea} - \partial_e g_{ac}\right) \\
&= \partial_a g_{bc} - \tfrac{1}{2}\left(\partial_a g_{bc} + \partial_b g_{ca} - \partial_c g_{ab}\right) - \tfrac{1}{2}\left(\partial_a g_{cb} + \partial_c g_{ba} - \partial_b g_{ac}\right) \\
&= 0.
\end{aligned}$$

We now use the fact that we can write the metric determinant as $g = \tfrac{1}{2}\varepsilon^{ab}\varepsilon^{cd} g_{ac} g_{bd}$. Here, ε^{ab} is the antisymmetric ε-symbol (which is 1 if ab is an even permutation of 12 and 0 otherwise). This is nothing but a fancy way of writing the Leibniz formula for determinants. But now we readily see that $\nabla_a g = 0$ immediately follows from $\nabla_a g_{bc} = 0$ and this equation, since the epsilon tensor is of course also a constant under differentiation.

2.2. Prove that the Gaussian curvature can be written as $K_G = \tfrac{1}{2}\left(K^2 - K_{ab}K^{ab}\right)$.

Answer

Since K^2 is the *square of the trace* of the curvature tensor, while $K_{ab}K^{ab}$ is the *trace of the square* of the curvature tensor, their difference can be written in terms of the eigenvalues c_1 and c_2 in the following way: $K^2 - K_{ab}K^{ab} = \left(c_1 + c_2\right)^2 - \left(c_1^2 + c_2^2\right) = 2c_1c_2$. Half of this is evidently the Gaussian curvature — the *product* of the two eigenvalues (which is identical to the *determinant* of the curvature tensor).

2.3. Show that the metric determinant is indeed given by the square of the modulus of the cross-product between the two tangent vectors, i.e., $g = \left|e_1 \times e_2\right|^2$.

Answer

Let α be the angle between $\mathbf{e}_1$ and $\mathbf{e}_2$. By using the definition of the metric as the matrix of scalar products between these vectors, we find

$$\begin{aligned}|\mathbf{e}_1 \times \mathbf{e}_2|^2 &= |\mathbf{e}_1|^2 |\mathbf{e}_2|^2 \sin^2\alpha = |\mathbf{e}_1|^2 |\mathbf{e}_2|^2 \left(1-\cos^2\alpha\right) = |\mathbf{e}_1|^2 |\mathbf{e}_2|^2 - \left(|\mathbf{e}_1||\mathbf{e}_2|\cos\alpha\right)^2 \\ &= |\mathbf{e}_1|^2 |\mathbf{e}_2|^2 - \left(\mathbf{e}_1 \cdot \mathbf{e}_2\right)^2 = g_{11}g_{22} - g_{12}g_{21} = g.\end{aligned}$$

2.4. Why is it true that $\mathbf{e}_a \cdot \partial_b \mathbf{n} = -\mathbf{n} \cdot \partial_b \mathbf{e}_a$?

Answer

Since the tangent vectors $\mathbf{e}_a$ are perpendicular to the normal vector **n**, their scalar product vanishes: $\mathbf{e}_a \cdot \mathbf{n} = 0$. Differentiating this orthogonality condition with respect to u^b (i.e., performing ∂_b on both sides) immediately leads to the equation above.

2.5. Given that the stretching modulus of typical phospholipid bilayers is $K_{\text{stretch}} \approx 250\ \text{mN/m}$, what value for Young's modulus of the membrane interior would this imply, if we make the simplifying assumptions that such an identification is permissible? Is that value reasonable?

Answer

Using $K_{\text{stretch}} = Yh$, where Y is Young's modulus and where $h \approx 4\ \text{nm}$ is the membrane thickness, we arrive at $Y \approx 60\ \text{MPa}$. This is a typical modulus for rubber. Given that rubbers are often dense polymer chains with characteristic length scales in the nanometer range, this modulus is indeed plausible.

2.6. Show that an incompressible material has a Poisson's ratio of $\nu = \frac{1}{2}$.

Answer

Recall that Poisson's ratio is the negative ratio between the relative transverse material deformation and the concomitant relative longitudinal deformation. Think now of a block of material of length L and square cross-section a^2. Its volume $V = La^2$ is supposed to remain constant under stretching. Hence we must have

$$0 = dV = d(La^2) = dLa^2 + L2a\,da = V\left(\frac{dL}{L} + 2\frac{da}{a}\right) = V\frac{dL}{L}\left(1 + 2\frac{da/a}{dL/L}\right) = V\frac{dL}{L}\left(1-2\nu\right) .$$

From this follows that $\nu = \frac{1}{2}$ must hold if the material is incompressible.

CHAPTER 3

3.1. Which lipid constitutes a better surfactant: triglyceride or DPPC?

Answer

Compare the hydrophobicity of lipids.

3.2. Depending on the temperature and surface pressure, lipid monolayers can form a variety of phases — e.g., gas, liquid-expanded, liquid-condensed, and condensed. At a fixed temperature and surface pressure, which monolayer has a higher molecular density: DPPC or POPC?

Answer

Compare the main phase transition temperatures of the bilayers.

3.3. The slope of the pressure–area isotherm gradually increases with increasing surface pressure. What can explain the decrease in isotherm slope at high pressures often observed experimentally?

Answer

Partial loss of lipids from the interface.

3.4. In simulations, molecular force fields often underestimate the surface tension at the water/vacuum interface. What is the possible result of a simulation, if the surface tension applied to the monolayer is larger than the surface tension at the water/vacuum interface (and smaller than the surface tension at the air/water interface in real systems).

Answer

Formation of pores in the monolayer; monolayer disruption if the applied tension is not achievable.

CHAPTER 4

4.1. What is the main driving force behind the concept of "Multiscale Modeling"?

Answer

Highly detailed models cannot describe large enough scales for collective motion. Even if possible, atomistic simulations would lead to information overkill. See further reading on multiscale modeling for more detailed information.

4.2. Which characteristics of supported bilayers are different or similar to free bilayers?

Answer

In general, the distal leaflet is very similar to a free bilayer, whereas the structure of the proximal leaflet is strongly influenced by the support. In comparison to real biomembranes, we always have to keep in mind that model membranes contain only a very limited subset of molecules.

4.3. Why are supported bilayers such an widely used model system?

Answer

Many experimental techniques are very difficult to directly apply to free bilayers (e.g., AFM). In addition, mechanical stability makes things much easier. Real membranes contain many constituents that make the analysis very complicated.

CHAPTER 5

5.1. In the chapter we discussed the overall process of pore-mediated lipid flip-flops and illustrated it for a dimyristoylphosphatidylcholine (DMPC) bilayer at $T = 323$ K. Make qualitative predictions regarding changes in the flip-flop rate when (a) temperature is decreased to e.g. the physiological value ($T = 310$ K); (b) DMPC lipids are replaced by dipalmitoylphosphatidylcholine (DPPC) lipids whose acyl chains are two hydrocarbons longer.

Answer

a. As there are no external forces applied to the bilayer system and the transmembrane lipid translocation across the bilayer is purely diffusive (driven exclusively by thermal fluctuations), one can expect that decreasing temperature should make the flip-flops slower and lead to a drop in the overall number of flip-flops, thereby decreasing the flip-flop rate. In contrast, increasing temperature will speed up flip-flop activity.

b. Longer hydrocarbon chains of DPPC lipids imply that a DPPC bilayer has a larger hydrophobic core than a DMPC does. This has two implications: (i) the energy required for pore formation and lipid desorption out of the monolayer (when a pore has been formed) is larger in the case of DPPC, and (ii) the pathway for lipid translocation is longer in a DPPC bilayer. Overall, both factors will lower the flip-flop rate for a DPPC bilayer as compared to the DMPC case.

   We note that the effects of temperature and acyl chain length on flip-flop activity were considered in detail in a very recent computational study of chemically induced lipid translocations across biological membranes [54].

5.2. Assuming that the lipid lateral diffusion coefficient is $D = 1 \times 10^{-7}$ cm^2/s, compute the time that is needed to diffuse from one side of a cell to the opposing one, assuming the cell radius to be R = 10 micrometers.

Answer

For diffusion in a plane, dimensional analysis yields $t = \ell_D^2 / D$, where ℓ_D is the length scale to be crossed. Assuming spherical cells, $\ell_D = \pi R$. Then the diffusion time asked is $t \approx 100$ s. The intriguing relationship here is the dependence of t on ℓ_D, that is, $t \propto \ell_D^2$. If the cell size was increased by a factor of 10, then the diffusion time would increase by a factor of 100, rendering diffusion of mass inefficient over a length scale of a cell. The fact that cells have a size of about tens of microns and the lipid diffusion coefficient is of the order of 10^{-7} cm^2/s implies mass diffusion to be efficient.

CHAPTER 6

6.1. Derive the cantilever amplification factor in the AFM detection system,

$$\Delta z = \frac{3L}{l}\Delta y \,, \tag{6.11}$$

where Δz is deflection of the laser spot when reaching the photodiode and Δy is the physical deflection of the cantilever end (see also §6.9).

Answer

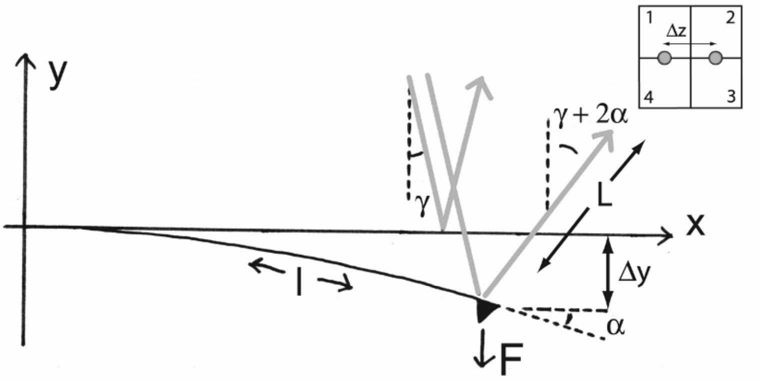

Figure 6.12.

Deflection of the laser spot is related to the cantilever bending angle as: $\Delta z = 2L\alpha$. The cantilever shape is given as a relation: $y(x)$. For small deflections ($\alpha \approx 0$) we have $\frac{dy}{dx} = \tan\alpha \simeq \alpha$, which means that

$$\Delta z = 2L\left[\frac{dy}{dx}\right]_{\text{end}} . \tag{6.12}$$

We consider the situation were a force F is applied to the tip at the cantilever end. The condition for static mechanical equilibrium is that for any value of x the torque $\tau(x)$ from internal stresses is equal to the torque due to force F:

$$\tau(x) = -F(l-x) = -\frac{EI}{R(x)} \Rightarrow \frac{1}{R(x)} = \frac{F(l-x)}{EI} \tag{6.13}$$

Where E is Young's modulus of the cantilever material, I is the *area moment of inertia* of the cantilever, and $R(x)$ is the curvature radius of the cantilever. When deflection α is small, the curvature radius can be written as

$$\frac{1}{R} = \frac{d^2 y}{dx^2}.$$

We therefore obtain

$$\frac{d^2 y}{dx^2} = \frac{F}{EI}(l - x). \tag{6.14}$$

When this differential equation is integrated with boundary conditions $[dy/dx]_{x=0} = 0$ and $y(x = 0) = 0$, we get the following equation for the cantilever shape, valid for small bending angles:

$$y(x) = \frac{F}{EI}\left(\frac{1}{6}x^3 - \frac{1}{2}lx^2\right). \tag{6.15}$$

Specifically, we can find the deflection Δy at the cantilever end:

$$\Delta y = y(l) = -\frac{Fl^3}{3EI}. \tag{6.16}$$

The deflection Δz of the reflected laser spot now becomes

$$\Delta z = 2L\left[\frac{dy}{dx}\right]_{x=l} = 2L\left[-\frac{Fl^2}{2EI}\right] = -\frac{Fl^2 L}{EI} = \frac{3L}{l}\Delta y. \tag{6.17}$$

From the last equality, we can conclude that vertical deflections of the cantilever are amplified by a factor $3L/l$ when measured in the photodiode detector.

6.2. Consider a situation where a fluorescence image is recorded of a double-membrane system with resolvable and superimposed domain features from membranes 1 and 2. The difference in partitioning of the fluorescence probe between the membrane domains generates contrast and gives rise to two intensities — high (H) and low (L) — from the two domains types, respectively. If we are only interested in analyzing the domain pattern in membrane 2, there is a potential problem in detecting these domain features without interference from membrane 1 domains. We will consider if and how this problem can be resolved.

a. Assume that the fluorescent intensity of the two domains is the same (H.L) in membrane 1 and 2. Will it be possible to detect domains in membrane 2 by simple threshold filtering (intensity cut-off)?

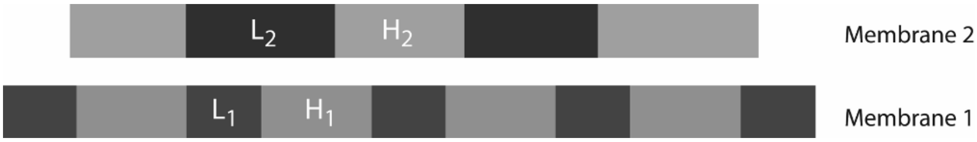

Figure 6.11.

b. Assume that the fluorescent intensity of the two domains is different (H_1,L_1,H_2,L_2) in membranes 1 and 2. Will it be possible to detect domains in membrane 2 by simple threshold filtering (intensity cutoff)? Will it be possible to detect the contour of islands in membrane 2? If yes, write down the restrictions on H_1,L_1,H_2,L_2 that enable these detections.
c. Discuss alternative experimental or computational tricks to improve domain detection in the above case.

Answer

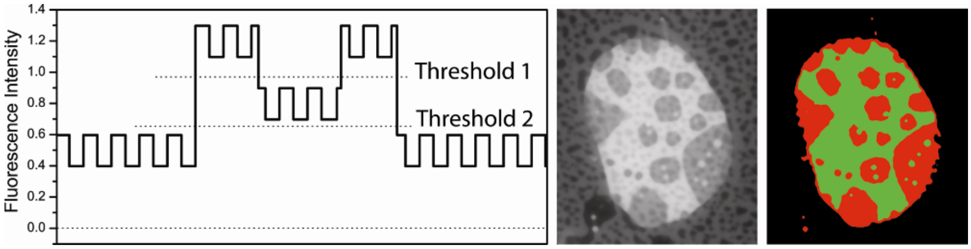

Figure 6.13. Please visit http://www.springer.com/series/7845 to view a high-resolution full-color version of this illustration.

Figure 6.13 shows schematically the fluorescence intensity of an image line crossing an island of membrane 2 on top of membrane 1. From the Figure 6.13 it can be seen that separation of domains within island 2, using threshold 1, implies the following inequality:

$$L_2 + H_1 < H_2 + L_1 \Rightarrow H_2 - L_2 > H_1 - L_1 . \tag{6.18}$$

Similarly, separation of the contour of island 2 from the background, using threshold 2, requires

$$L_1 + L_2 > H_1 \Rightarrow H_1 - L_1 < L_2 . \tag{6.19}$$

As an example, the figure illustrates the fulfillment of these conditions by the intensities (H_1,L_1,H_2,L_2) = (0.6, 0.4, 0.7, 0.3). Regarding Problem 6.2a, it is clear that domain detection by thresholding is not possible if $H_1 = H_2$ and $L_1 = L_2$ (but detection of island contour is). Simply speaking, this result shows that domain detection in membrane 2 is possible if the intensity contrast is larger than that in membrane 1. In certain cases [34], we have found that membrane–solid interactions in membrane 1 are sufficient to alter domain contrast compared to membrane 2 and enable domain detection, as described above. An example of this is shown in Figure 6.13, demonstrating threshold detection of the island boundary and of domains within the island without interference from domain features in the underlying membrane.

CHAPTER 7

7.1. Why is ionic current reduced when a single-stranded nucleic acid molecule traverses a nanopore?

Answer

The open-channel ionic current is carried through the nanopore by the electrolyte ions present in the solution. In a typical configuration using Ag/AgCl electrodes and a KCl solution, the current is carried by K^+ and Cl^- ions. When a single-stranded nucleic acid molecule enters and traverses the pore, it reduces the volume of electrolyte available for the flux of ions, thus reducing the ionic current. In addition, if the macromolecule is negatively charged, as is the case with nucleic acids, it introduces a significant negative charge density into the pore that largely prevents the flux of Cl- ions. The ionic current blockade is also related to the salt concentration used to carry the current, and it is possible to find conditions in which the translocation of nucleic acids actually increases the ionic current during translocation. This has been observed in solid-state nanopores at low salt concentrations. In this case, current increases are due to the counterions that screen the charge of the DNA backbone [40].

7.2. A homopolymer molecule such as polydeoxycytidylic acid, 100 bases in length, requires an average of 0.2 ms to traverse the pore.

a. How much time does an individual base spend in the pore?
b. Given that this time is too short for identification of individual bases, what can be done to slow down the translocation velocity?

Answer

a. About 2 μs [5].
b. A number of strategies can be used to reduce the translocation speed of macromolecules through nanopores. These include increasing the viscosity of the medium (e.g., by using glycerol), reducing the applied voltage, and reducing the temperature [41]. The most dramatic reduction was achieved when a nucleic acid processing enzyme such as an exonuclease or polymerase binds to the DNA and is drawn to the pore as a complex [26,27].

CHAPTER 8

8.1. In an FRAP experiment, the scaled fluorescence intensities are $F_i = 1$, $F_0 = 0.4$, and $F_\infty = 0.8$. Assume the bleaching spot is a disk with radius 1 μm and the half time of recovery (τ_D) is 0.2 s.

a. Find the diffusion coefficient for this protein. (Assume a uniform circular laser profile.)

b. Find the mobile and immobile fractions of this protein.

Answer

a. From Eq. (8.23), $D = 0.22\frac{1^2}{0.2} = 1.1$ μm²/s.

b. From Eq. (8.23):

$$\mathrm{MF} = \frac{F_\infty - F_0}{F_i - F_0} = \frac{0.8-0.4}{1-0.4} = \frac{2}{3}, \quad \mathrm{IF} = \frac{F_i - F_\infty}{F_i - F_0} = \frac{1-0.8}{1-0.4} = \frac{1}{3}.$$

8.2. Two FRAP experiments were performed for the same protein using circular ROIs of different size. The half times of recovery (τ_D) were 0.5 and 1 s. What is the ratio of the ROI radii in two experiments? (Assume a uniform circular laser profile.)

Answer

From Eq. (8.23), $0.22\frac{\omega_1^2}{0.5} = 0.22\frac{\omega_2^2}{1} \Rightarrow \frac{\omega_1}{\omega_2} = \sqrt{\frac{0.5}{1}} \simeq 0.71$.

8.3. If the diffusion coefficient of a protein X is approximately 40 μm²/s, what is the expected half time of recovery for a circular ROI with a 10-pixel diameter? (Assume a uniform circular laser profile and 1 pixel = 0.11 μm).

Answer

From Eq. (8.23), $40 = 0.22\frac{(5\times 0.11)^2}{\tau_{1/2}} \Rightarrow \tau_{1/2} = 0.22\frac{(5\times 0.11)^2}{40}$.

8.4. For two soluble proteins X and Y with molecular weights W_x and W_y and diffusion coefficients D_x and D_y, respectively, derive the following relation from the Stokes-Einstein equation. (Assume the shapes of these proteins are spherical.)

a. $D_y = D_x\sqrt[3]{\frac{W_x}{W_y}}$.

b. If the molecular weight of X is 27 kDa, and the diffusion coefficient of X is 10 μm²/s, what is the expected diffusion coefficient of a protein with a molecular weight of 40 kDa?

Answer

a. From Eq. (8.13), $D = \dfrac{\kappa_B T}{6\pi\eta r}$. If we assume that the shapes of proteins are spherical and that the molecular weights are directly proportional to the volumes of proteins, we get $r_x = \sqrt[3]{W_x}$. Therefore,

$$\frac{Dx}{Dy} = \frac{r_y}{r_x} = \frac{\sqrt[3]{W_y}}{\sqrt[3]{W_x}} \Rightarrow Dx = Dy\sqrt[3]{W_y / W_x} .$$

b. From (a), $Dx = Dy\sqrt[3]{W_y / W_x} \Rightarrow Dx = 10\sqrt[3]{27/40}$.

8.5. For Eq. (8.24), assume $D_2 \neq 0$ and $k_{\text{on}} \gg D_1/(4\omega^2),\ D_2/(4\omega^2)$. D_2 may not necessarily be smaller than D_1.

a. Show that Eq. (8.24) can be approximated by the effective diffusion model with an effective diffusion coefficient

$$D_{\text{eff}} = \frac{k_{\text{off}} D_1 + k_{\text{on}} D_2}{k_{\text{on}} + k_{\text{off}}} .$$

b. From this show that the partition coefficient ($k_p = k_{\text{on}}/k_{\text{off}}$) is given by $k_p = \dfrac{D_1 - D_{\text{eff}}}{D_{\text{eff}} - D_2}$.

Answer

a. From

$$\begin{cases} \dfrac{\partial u}{\partial t} = D_1 \nabla^2 u - k_{\text{on}} u + k_{\text{off}} c \\ \dfrac{\partial c}{\partial t} = D_2 \nabla^2 c + k_{\text{on}} u - k_{\text{off}} c \end{cases},$$

adding the two we get, $\dfrac{\partial}{\partial t}(u + c) = D_1 \nabla^2 u + D_2 \nabla^2 c$. Because binding is fast compared to diffusion, a local chemical equilibrium $c = \dfrac{k_{\text{on}}}{k_{\text{off}}} u$ is expected, i.e.,

$$\frac{\partial}{\partial t}\left(u + \frac{k_{\text{on}}}{k_{\text{off}}} u\right) = D_1 \nabla^2 u + \frac{k_{\text{on}}}{k_{\text{off}}} D_2 \nabla^2 u \Rightarrow \left(1 + \frac{k_{\text{on}}}{k_{\text{off}}}\right)\frac{\partial}{\partial t} = \left(D_1 + \frac{k_{\text{on}}}{k_{\text{off}}} D_2\right)\nabla^2 u$$

$$\Rightarrow \frac{\partial u}{\partial t} = \left(\frac{k_{\text{on}} D_1 + k_{\text{off}} D_2}{k_{\text{on}} + k_{\text{off}}}\right)\nabla^2 u .$$

b. This can be done by solving $D_{\text{eff}} = \dfrac{k_{\text{off}} D_1 + k_{\text{on}} D_2}{k_{\text{on}} + k_{\text{off}}} = \dfrac{D_1 + k_p D_2}{1 + k_p}$ for k_p.

8.6. If Eq. (8.24) is in the reaction-dominant regime, the concentration of fluorescence intensity is represented in terms of binding complex concentration, $c(x,y,t) \simeq c_i\left(1-e^{\kappa_{\text{off}} t'}\right)$. From this and employing $F(t) = q\varepsilon \iint_{\mathbb{R}^2} I(x,y)C(x,y,t)\,dx\,dy$, derive the corresponding FRAP formula.

Answer

$$\begin{aligned} F(t) &= q\varepsilon \iint_{\mathbb{R}^2} I(x,y)C(x,y,t)\,dx\,dy \\ &= q\varepsilon \iint_{\mathbb{R}^2} I(x,y)\left[C_i\left(1-e^{k_{\text{off}} t}\right)\right]dx\,dy \\ &= \left[q\varepsilon C_i\left(1-e^{k_{\text{off}} t}\right)\right]\iint_{\mathbb{R}^2} I(x,y)\,dx\,dy \\ &= F_i\left(1-e^{k_{\text{off}} t}\right). \end{aligned}$$

CHAPTER 9

9.1. Free energy of a pore: line tension and surface tension.

a. Let us consider a membrane with a surface tension γ. What is the cost in free energy, E, for the creation of a pore of radius R, if the line tension along the edge of the pore is λ?

b. How does ΔE vary with R? What does this imply about the stability of the pores?

c. What is the surface tension in a biological membrane? What does it imply for pore formation?

Answers

a, The formation of a pore corresponds to a reduction in the membrane surface area, $\Delta A = -\pi R^2$, and to the creation of a membrane edge of length $\Delta L = 2\pi R$. Therefore the free energy associated with the formation of the pore is

$$\Delta E(R) = -\pi R^2 \gamma + 2\pi R \lambda \ .$$

The existence of a positive surface tension favors pore formation, whereas the existence of a line tension discourages pore formation.

b. Assuming the surface and line tensions are constant, the free energy of the pore is maximum for a pore radius $R_0 = \lambda/\gamma$. Thus, in this particular situation, pores are never stable: small pores ($R < R_0$) close rapidly whereas large pores ($R > R_0$) keep increasing in size indefinitely.

c. In general, a relaxed biological membrane has a negligible surface tension. According to the equation above, pore formation in a relaxed membrane requires an input of energy of at least $2\pi R\lambda$. If this energy is larger than the thermal energy kT, pores will not appear spontaneously in this type of membranes. On the other hand, if a tension is imposed on the membrane (e.g., using micropipette aspiration [234,235], osmotic stress [236], or electroporation [237]), the spontaneous formation of pores becomes possible.

9.2. Free energy of a water-filled membrane channel. We first consider a hypothetic type of water-filled channel, where the lipids do not rearrange themselves along the edge of the pore, as illustrated in Figure 9.8A, in a relaxed membrane for which the surface tension is $\gamma = 0$.

a. Find the expression for the line tension at the edge of the pore as a function of the thickness of the hydrophobic part of the bilayer, h_C, and the surface tension between the apolar medium formed by the lipid carbon chains and the polar water solvent, γ_C.
b. The typical thickness of the hydrophobic part of a phospholipid bilayer is $h_C = 3$ nm, and the value of the surface tension between oil and water is $\gamma_C \approx 50$ mN/m. Estimate the free energy associated with the formation of a pore of radius $R = 1$ nm.
c. Can such pores form spontaneously in biological membranes?

Answers

a. The main energy cost associated with the creation of a water-filled channel such as the one depicted in Figure 9.8A comes from the formation of a contact area between the apolar lipid hydrocarbon chains and the polar water solvent. The line tension for such a pore therefore corresponds to the surface energy of a polar/apolar interface with height h_C and with unit length:

$$\lambda = h_C \gamma_C \, .$$

b. Given $h_C = 3$ nm, and $\gamma_C = 50$ mN/m, we find a line tension for this type of pore of $\lambda = 150$ pN. The formation of a pore of radius $R = 1$ nm will therefore cost $\Delta E = 2\pi R\lambda \sim 10^{-18}$ J.
c. If we compare ΔE to the thermal energy at room temperature, $k_B T \sim 4 \times 10^{-21}$ J, we see that $\Delta E \sim 250\ k_B T$. Therefore,, spontaneous pore formation is very unlikely.

9.3. Free energy of a toroidal pore. We next consider a more realistic model for the pores, where the lipid surface curves in order to connect the two membrane leaflets (toroidal pore), as illustrated in Figure 9.8B.

a. At the pore, what is the curvature, C_1, of the lipid surface in a plane perpendicular to the membrane? What is the curvature, C_2, in a plane parallel to the membrane? Which of these two membrane deformations is the more energetically costly?
b. By considering only the most costly type of curvature, give an expression for the line tension associated with the edge of the pore as a function of the pore radius, R, the bilayer thickness, h, and the bending modulus of the lipid monolayer, k_C.
c. The bending modulus of a lipid monolayer can be estimated to be half that of the lipid bilayer, leading to $k_C \approx 2 \times 10^{-20}\,\mathrm{J}$ [233]. Estimate the free energy associated with the formation of a toroidal pore with radius $R = 1$ nm,
d. Can such pores form spontaneously in biological membranes?

Answers

a. In a toroidal pore, the lipid surface both has a positive curvature (in planes perpendicular to the plane of the membrane) and a negative curvature (in planes parallel to the plane of the membrane. The positive curvature is constant, $C_1 = 2/h$ (where h is the total membrane thickness). The negative curvature on the other hand, goes from 0 at the top and bottom of the pore, to $C_2 = -1/R$ in its center. Since phospholipids have a bulky hydrophobic tail, a positive curvature of the lipid surface is usually more costly than a negative curvature.

b. Considering only the cost of the positive curvature of the membrane, we see that the curved surface, S, corresponds to half the surface of a torus, thus, $S = \pi^2(R + h/2)h$. The line tension corresponds to the bending energy of a unit length stretch of the pore edge:

$$\lambda = \frac{1}{2\pi R}\frac{1}{2}k_C C_1^2 S = \pi k_C \frac{R+h/2}{Rh}.$$

c. For $R = 1$ nm, $h \sim 3$ nm, and $k_C \sim 2 \times 10^{-20}$ J, we get $\lambda = 50$ pN, and in the limit of large pore diameters we obtain $\lambda = \pi k_C/h = 20$ pN. This value is in reasonable agreement with the experimental values for the line tension of membrane pores, which range from 3 to 30 pN [235,238–240]. The corresponding energy (for $R =$ 1 nm) is $\Delta E = 2\pi R\lambda \sim 3 \times 10^{-19}$ J $\sim 80\ k_BT$.

d. The energy cost to form a toroidal pore is still too high for these pores to form spontaneously in a relaxed membrane.

9.4. Reduction of pore free energy by pore-forming proteins. We now consider the stabilization effect that PFPs have on membrane pores, by adapting a model originally developed by Huang et al. for antimicrobial peptides [222]. The premise of this model is that the pore-forming protein (present at a total surface concentration c) can exist in two different membrane states: either as a partially inserted monomer (concentration αc), or as part of an oligomeric membrane pore. Monomeric proteins both increase the surface area of the membrane leaflet in which they insert (each by an amount A_m), and induce a positive tension in the membrane, $\gamma = \gamma_0 A_m \alpha c$. Oligomeric proteins are lining the pores, and although the pore size may vary, the linear density of protein along the edge, ρ, is constant, so that the line tension at the pore, λ, is also constant. This model is therefore better adapted to PFPs for which the pore size and stoichiometry vary with the protein concentration, typically α-PPFs.

a. If ε_m is the binding energy of a monomeric PFP and ε_o is the pore energy per protein lining the pore, what is the free energy per unit area, F, of the system constituted by the lipids and the proteins? Use this to show that above a critical concentration of proteins in the membrane, c^*, the concentration of monomeric protein remains constant.

b. Consider that $c > c^*$, and that pores exist on the membrane at a concentration C. Write the expression for the free energy of a single pore, ΔE, as a function of its radius, R.

c. How many energy minima are there for a single pore, and which radius do they correspond to? Are those energy minima stable or unstable? Explain the origin of the pore stabilization according to this model.

d. In addition to influencing the membrane surface tension, the PFPs also reduce the line tension of the pores. How does reducing the line tension further influence the structure and/or stability of the pores?

Answers

a. In the absence of a tension other than that produced by the insertion of the monomeric protein, the free energy per unit area of the system formed by the lipids and the proteins is

$$F = \varepsilon_{\mathrm{m}} \alpha c + \varepsilon_0 (1-\alpha) c + \frac{1}{2} \gamma_0 (A_{\mathrm{m}} \alpha c)^2 .$$

The first term corresponds to the binding energy of the fraction of proteins that are monomeric and the second term to the energy of the pores. The third term is the increase in membrane energy after the membrane surface has increased by the relative amount $\delta A/A = A_{\mathrm{m}} \alpha c$, while acquiring a positive tension $\gamma = \gamma_0 A_{\mathrm{m}} \alpha c$.

Deriving F with respect to α shows that the minimum value of this free energy is obtained for

$$\alpha c = \frac{\varepsilon_0 - \varepsilon_{\mathrm{m}}}{\gamma_0 A_{\mathrm{m}}^2} .$$

If $\varepsilon_{\mathrm{o}} < \varepsilon_{\mathrm{m}}$, this condition cannot be fulfilled (as α cannot be negative), and we simply have $\alpha = 0$: all the proteins are part of a pore. On the other hand, if $\varepsilon_{\mathrm{o}} > \varepsilon_{\mathrm{m}}$, then this condition can be fulfilled as long as $\varepsilon_{\mathrm{o}} - \varepsilon_{\mathrm{m}} < \gamma_0 A_{\mathrm{m}}^2 c$ (as α cannot exceed 1). We define c^* as

$$c^* = \frac{\varepsilon_0 - \varepsilon_{\mathrm{m}}}{\gamma_0 A_{\mathrm{m}}^2} .$$

If $c < c^*$, then $\alpha = 1$, meaning that all the proteins on the membrane are found as monomers. If $c > c^*$, then $\alpha = c^*/c$, meaning that the concentration of monomeric proteins on the membrane is constant (and equal to c^*), while the concentration of proteins that are part of a pore is equal to $c - c^*$.

b. The energy of a pore, ΔE, is the sum of two contributions, just as in Problem 9.1a, but this time the tension in the membrane depends on the fraction of monomeric protein, $\gamma = \gamma_0 A_{\mathrm{m}} \alpha c$. And since $\alpha c = c - (1-\alpha) c = c - 2\pi R \rho C$, the membrane tension is related to the concentration, C, and radius, R, of the pores:

$$\gamma = \gamma_0 A_{\mathrm{m}} c - 2\pi \gamma_0 A_{\mathrm{m}} \rho C R .$$

Since we cannot assume that the surface tension is constant, in order to calculate ΔE we first need to consider the small change in energy, δE, associated with a small change in pore radius, δR:

$$\delta E = \lambda 2\pi\delta R - \gamma 2\pi R\delta R = 2\pi\lambda\delta R - 2\pi\gamma_0 A_{\mathrm{m}} cR\delta R + 4\pi^2\gamma_0 A_{\mathrm{m}}\rho CR^2\delta R\,.$$

Integrating this expression, we obtain the energy of a single pore of radius R:

$$E(R) = 2\pi\lambda R - \pi\gamma_0 A_{\mathrm{m}} cR^2 + \frac{4}{3}\pi^2\gamma_0 A_{\mathrm{m}}\rho CR^3\,.$$

c. As it is third-order in R, the energy $E(R)$ has two extrema. The first corresponds to a local maximum for R equal to

$$R_{\mathrm{M}} = \frac{c}{4\pi\rho C}\left[1 - \sqrt{1 - \frac{8\pi\rho C}{\gamma_0 A_{\mathrm{m}} c^2}\lambda}\,\right].$$

The second corresponds to a local minimum for R equal to

$$R_{\mathrm{m}} = \frac{c}{4\pi\rho C}\left[1 + \sqrt{1 - \frac{8\pi\rho C}{\gamma_0 A_{\mathrm{m}} c^2}\lambda}\,\right].$$

This local minimum corresponds to a stable finite value of the pore radius. Given that R cannot be negative, $R = 0$ (no pore) also corresponds to a stable state.

According to this model, creation of the pores is due to the presence of monomeric proteins in the membrane, which create a positive surface tension. The stabilization of the pores comes from the fact that when the pores grow the concentration of monomers in the membrane decreases, and so does the membrane tension, which creates a negative feedback on the size of the pores.

d. For R_{m} to be a real number, the line tension of the pore needs to be small enough:

$$\lambda \le \lambda^* = \frac{\gamma_0 A_{\mathrm{m}} c^2}{8\pi\rho C}\,.$$

Therefore, reducing the surface tension of the pores is another important mechanism by which PFPs can promote pore formation: If $\lambda > \lambda^*$ there is no stable solution for the diameter of the pore other than $R = 0$. The line tension also directly influences the structure of the pores: if λ decreases, R_{m} increases.

CHAPTER 10

10.1. **Case Study of Human BMP 2 and Fracture Healing**. Patients ($n = 450$) with an open tibial fracture were involved in randomized, single-blind study. The study was conducted at 49 centers in 11 countries. Patients were prospectively randomized to one of three groups. Patients who met the study eligibility had provided informed consent and had been properly randomized irrespective of whether they received treatment:

Group 1 — received standard of care (SOC) (intramedullary nail fixation), which was the control group
Group 2 — received rhBMP-2 (0. 75 mg/ml)
Group 3 — received intramedullary nail fixation and BMP 2.

Treatments were assigned to each group. They were followed after the treatment for the following lengths of time: 6, 10, 14, 20, 26, 39, and 52 weeks after treatment.

A fracture was considered to be healed when there was radiographic evidence of fracture union and met all the clinical criteria. The primary outcome measure was the recommendation of secondary intervention because of delayed union or nonunion within 12 months postoperatively. All interventions were classified according to the degree of invasiveness.

Which of the three groups will report a shorter time to fracture union and why?

Answer

Consult the following: Govender S. 2002. Recombinant human bone morphogenetic protein-2 for treatment of open tibial fractures: a prospective, controlled, randomized study of four hundred and fifty patients by the BMP-2 evaluation in surgery for tibial trauma. *J Bone Joint Surg* **84**:2123–2134.

Control Group 1: fractures were united after 6 months.

Groups 2 and 3: there was a consistent increase in the rate of healing starting at 10 weeks after definitive wound closure.

At 6 months the healing rate observed between the control group and Groups 2 and 3 was 21% higher in Groups 2 and 3. The rate of fracture healing was accelerated in Groups 2 and 3 as compared to the control group.

CHAPTER 11

11.1. How can apoE conformation be used clinically to detect vascular inflammation and atherosclerosis?

Answer

Apolipoprotein E4 reports on the local lipid environment to which it is associated. Conformation of apoE4 also could signify likelihood of binding to and injure of vascular cells. Thus, apoE4 conformation could become a biomarker for prediction of risk for atherosclerotic cardiovascular disease (see [9]).

CHAPTER 12

1. Patients with familial hypercholesterolemia (FH) have a defective biosynthesis of LDL receptors or dysfunctional LDL receptors. As a consequence, cholesterol levels rise dramatically in the serum, and FH patients suffer from cardiovascular diseases at an early

age. Statins reduce serum cholesterol by competitively inhibiting hepatic HMG-CoA reductase, the enzyme catalyzing the committed step in cholesterol biosynthesis in the liver. By decreasing cholesterol synthesis, a non-FH cell would have more available LDL receptors to reduce serum cholesterol level. But FH patients have no LDL or dysfunctional receptors. A statin drug, such as atorvastatin, would not alter the number of available LDL receptors by inhibiting HMG-CoA reductatse activity and therefore would not reduce an FH patient's serum cholesterol level.

2. See the following articles:

Kaysen GA 2006. Dyslipidemia in chronic kidney disease: causes and consequences. *Kidney Int* **70**:555–558.

Hovingh GK, de Groot E, van der SW, Boekholdt SM, Hutten BA, Kuivenhoven JA, Kastelein JJ. 2005. Inherited disorders of HDL metabolism and atherosclerosis. *Curr Opin Lipidol* **16**(2):139–145.

INDEX

α-helical hairpin, 227, 247
α-hemolysin, 230–232, 235–236, 238, 240
    as biological nanopore, 171–174, 181–182
α-PFPs, 226–230, 248–249
    fluorescence and, 240–241
α-synuclein, 230, 244, 248
ABCAI (ATP-binding cassette transporter AI), 289
Absorption spectrum of fluorophore, 191
Actinosporins, 230
Activation in pore formation, 246
Activation peptide, 246
Active transport of lipids across membranes, 123
Adsorption in inhomogeneous system, 7
Aerolysin, 237, 249
Air/water interface of lipid monolayers, 77
    simulation, 87–89
Alamethicin, 234
Alcohols affecting lipid structure, 22–24
Alcohols affecting mechanical properties, 32–33
Amphipathic cationic α-helices, 25
Amphipathic sequences in pore-forming proteins, 225
Amphiphilic lipids, 4, 77
Amyloid diseases, 230
Anisotropic stress, 57
Anomalous diffusion, 211–215
Anthrax protective antigen, 237, 246, 249
Anthrax toxin, 233
Antigen, protective of anthrax toxin, 233
Antimicrobial peptides, 25, 225, 236, 237, 243
Apolipoprotein (apoA-I), 289
    imaging in vivo, 293
    therapy, 289–290
Apolipoproteins, 278–279, 289
    and cardiovascular disease risk, 288–289
    imaging using magnetic resonance, 290–293
Area compressibility modulus, 29, 79, 93
    affected by alcohols, 32–33
Area difference elasticity, 51
Area isotherms, 85
Area per lipid molecule, 90
Aromatic belt, 235, 244–245
Aromatic residues in proteinaceous pores, 235
Articular cartilage, 265. *See also* Cartilage
Asymmetric pressure distribution, 78
Asymmetric transmembrane lipid distribution, 123–124
Atomic force microscopy (AFM), 84–85
    for determining pores, 239
    for imaging supported membranes, 154–156
Atomistic models, 103
    and force fields, 87
ATPase P4, 181

β-hairpin, 232, 235
β-PFPs, 224, 227, 230–233, 248–249
β-sheet, 230
Barrel-stave model of pores, 234–235
Bax, 237, 241, 248–249
Bcl-2 family of pore-forming proteins, 229–230
Bead-spring models, 6
Bending energy in membrane bilayers, 44–46
Bending modulus, 29
Bessel function, 64–66
Bilayer elasticity, 43–47
Bilayer formation during spin coating, 149
Bilayer thickness, 17, 23–24
Binary model membranes, 161–162
Binding-diffusion model of FRAP, 205–211
Binding site of membranes, 205
Biomembranes, continuum theory for, 43–47
Biophysics, scale separation in, 41–43
Biphasic model of FRAP, 209–211
Boltzmann distribution, 11
Bone morphogenetic proteins (BMPs), 264, 266, 269
Boundary conditions in membrane interactions, 63
Brewster angle microscopy, 84
Butanol, 23–24, 32–33

Cantilever bending in atomic force microscopy, 154–155
Captive bubble surfactometer, 85
Cardiovascular disease risk, 288
    and apoA-I therapy, 289–290
    and apoproteins, 288–289
Cartilage, 267–268. *See also* Articular cartilage
    morphogenesis, 264
Caspase activation, 229
Catalytic domain in diphtheria toxin, 228
Cavity correlation functions, 13–14
Cell membrane and mechanotransduction, 266–268
Centers of mass (CM) of lipid headgroups, 130–132
Ceramide in membranes, 161
CHARMM force field, 89–90, 105
Chemical potential of inhomogeneous system, 10
Cholesterol, 76, 244, xix
    balance, 288–289
    complexing with phospholipids, xvii–xxi
    scavenging by high density lipoprotein (HDL), 287–288
    transported by low density lipoprotein (LDL), 286–287

Cholesterol-dependent cytolysins, 232
Cholesteryl ester transfer protein (CETP), 287
Chondrocytes, 268–269
  and transforming growth factor (TGF-β) superfamily, 265–266
Christoffel symbol, 49
Chylomicrons, 279, 287
  and triacylglycerol, 286
Closed-loop phase diagrams for ternary lipid mixtures, xviii–xix
CMS-DFT, 8–12, 22
Coarse-grained (CG) lipid model, 2, 5–6
  and bilayer properties, 18–19
  energetics of, 14–15
  and force fields, 87
  of lipid bilayers, 103
Coherent anti-Stokes Raman scattering (CARS) microscopy, 282
Colicins, 228, 247, 248
Collagen, 265
Collapse pressure, 81
Composition-dependent spontaneous curvature, 52
Compression/expansion cycling, 93
Compression in articular cartilage, 267
Computer simulations of lipid monolayers, 86–95
Condensed complexes, xviii
Condensed (C) phase of lipid monolayers, 80–81
Confocal fluorescence microscope, 193–194
Confocal FRAP, 215–218
Confocal microscopy, 159
Conservation of mass, 197–198
Consistency conditions, 55
Contact-mode scanning in atomic force microscopy, 155
Continuous-time random walk model, 211
Continuum elasticity theory, 43
Continuum-level theories, 2
Continuum theory for biomembranes, 43–47
Contrast in microscopy, 153
Coulomb potential, 86
Cry δ-endotoxins, 229
Cryo-EM, 238–239
Curvature-dependent free energy, 2
Curvature elasticity, 47–53
Curvature-mediated force, 62
Curvature stress, 58
Curvature tensor, 48, 58
Cylindrical micelles, 43
Cyt δ-endotoxins, 242
Cytokines in cartilage, 266
Cytolysins, 244, 247, 249
Cytolysins, cholesterol-dependent, 232

δ-endotoxin, 247
Decorated lattice models, xx–xxi
Density distribution in lipid/solvent systems, 11
Density functional theory, 6
Density profiles, 6–7
  for bilayers with added alcohols, 22–24
  in CMS-DFT, 10–11, 22
  of equilibrium system, 8–9
  of model lipid bilayers, 19–21
  of supported lipid bilayers, 107–108, 110–113
  of zero tension bilayer, 17–18
Dewetting in spin coating, 148
Dichroic mirror, 193–194
Dielectrophoretic force in flip-flops, 134
Diffusion, 211–215
  and fluorescence, 197–199
  during photobleaching, 215–216
Diffusion coefficient, 122, 188, 198, 203–204, 216
Diffusion-dominant model of FRAP, 207–208
Diffusion equation, 199–200
Dimerization of nuclear receptors, 241
Dimyristoylphosphatidylcholine (DMPC) lipids, 124
Dioleoylphosphatidylcholine (DOPC), xix
Dipalmitoylphosphatidylcholine (DPPC), 18, xix
  atomistic modeling of, 104–105
  mesoscale modeling of, 105–106, 109
  monolayer studies of, 91–92
  pressure profile of, 113–114
  surface pressure-area isotherm of, 92–93
Diphtheria toxin, 228–229
Direct correlation function, 10
Distal leaflet, 108, 110–113
DLVO (Derjaguin, Landau, Verwey, Overbeek) theory, 151–152
DNA hairpin molecules, 176–179
DNA in nucleic acids blockades, 173–174
DNA processing enzymes and nanopore analysis, 180–182
Domain coarsening, 163–164
Domains in model membranes, 159–160
Double-bilayer lipid system, 124–125
Double layer repulsion, 152
Dynamics in lipid membranes, 121–136
Dyslipidemia, 288

Effective diffusion coefficient, 209
Einstein-Stokes equation, 199
Einstein tensor, 58
Elastic constants, 29–30, 47, 52
Elasticity, curvature, 47–53
Elasticity theory, 2
Electromagnetic radiation, 188–189
Electron microscopy for determining PFPs, 238–239
Electrostatic double layer energy, 151
Electrostatic interactions between protein and membrane, 89, 243–244
Embedding function, 54–55
Emission spectrum of fluorophore, 191
Endothelial layer permeability, 280
Energy density, 51–52
Energy levels in fluorescence, 190–191
Epifluorescence microscopy, 157–158
Equations of Gauss-Codazzi-Mainardi, 49–50
Equilibrium density profile, 6–7
Equilibrium fluid density profiles, 17–18
Equilibrium properties of membranes, 3
Equilibrium spreading pressure, 77

Equinatoxin II, 230, 237
Ethanol, 23–24
    affecting mechanical properties, 32–33
Euler-Lagrange equation, 54–57, 59, 64, 65, 67
Excess surface free energy, 28–29
Excitation light, 197
Exotoxin, 237
External potential of systems, 6–7
Extracellular matrix (ECM), 265
    and mechanotransduction, 266–268
Extrinsic curvature, 48

Familial hypercholesteremia, 287
Feder's model of anomalous diffusion, 213
Fick's first law, 197–198
Film thickness in spin coating, 146–147
Flexible lipid models, 5
Flip-flops of lipids in membranes, 123–124, 129–135
Flippases, 123
Fluid-mosaic model, 142
Fluids density functional theories, 6–14
    calculations for model lipid bilayers, 16–17
    CMS-DF, 8–12, 22
    modified i-SAFT, 12–14, 22
Fluids-DFTs. *See* Fluids density functional theories
Fluorescein isothiocyanate (FITC) immunofluorescencee, 188
Fluorescence, 188–192
    for determining PFPs, 239–241
    origin of, 190–192
    recovery by diffusion, 197–199
Fluorescence emission, 191
Fluorescence fluctuation analysis, 241
Fluorescence intensity (FI), 188
Fluorescence intensity distribution analysis (FIDA), 241
Fluorescence lifetime, 191
Fluorescence microscopy (FM), 84, 157–159, 188
Fluorescence Recovery after Photobleaching. *See* FRAP
Fluorescence resonance energy transfer (FRET), 240
Fluorescent intensity, 201–203
Fluorophore, 190
    absorption spectrum, 191
    emission spectrum, 191
Force fields in lipid monolayers, 86, 87, 89–90
Fourier-Laplace transform, 214
Fourier transform, 199
Fractional-diffusion model of anomalous diffusion, 213–215
FRAP, 205–215
    curves, 203–204
    mathematical model of, 197–201
Free energy of equilibrium, 29–32
Free energy of systems, 6–8
Fundamental measure theories (FMT), 8

γ-hemolysins, 231–232
Gadolinium-diethylenetriaminepentaacetic acid, 290–293
Gadolinium-methanethiosulfonate, 290–291
Gas phase of lipid monolayers, 79–81
Gaussian curvature, 48, 50
Gaussian laser beam, 200, 204
Gaussian laser beam profile, 195–196
Gaussian modulus, 58
Ginzburg-Landau energy, 56–57
Glass as membrane support material, 145
Glycerophospholipids, 76, 77
Glycosaminoglycans (GAGs), 265
Gouy-Chapman theory, 243
Gramicidin, 237
Grand free energy density, 30
Graphite, 104
Green fluorescent protein (GFP), 188
Growth factors, 264–266, 268–269

Hamaker constant, 152, 153
Hamiltonian, 52, 58
Hard sphere fluid and density functional theory, 12–14
Hard sphere models, 8
Head-tail interface in lateral pressure, 31–32
Headgroup–headgroup interactions, 77
Headgroup–solvent interface, 25–28
Headgroup–tailgroup interfaces, 8, 23–24
Headgroup volume ratio to tail volume, 18
Headgroups, 15
    role in lipid monolayer curvature, 245
Heavy tail distribution, 212
Helmholtz equation, 64
Helmholtz free energy, 6, 9, 12, 13
Hemolysin nanopore, 171–174, 181–182
Hexagonal packing, 80, 93, 107
Hexanol in lipid bilayers, 23–24, 32–33
High density lipoprotein (HDL), 289
    and cholesterol scavenging, 287–288
HMG-CoA, 288
Homopolymers of nucleic acids, detection of, 173–175
Hooke's law for curvatures, 44, 45
Hydration forces in membrane support, 152
Hydrocarbon chains, 76, 78
    unsaturation, 76
Hydrogen bond network in bilayer formation, 149
Hydrophilic headgroup of lipids, 76
Hydrophobic hairpin in pore-forming proteins, 227–228
Hydrophobic patches, 246
Hydrophobic tail of lipids, 76

i-SAFT, 12–14, 22
Imaging membrane microstructure, 153–154
Implicit solvent models, 5
Inhomogeneity of fluids, 6
Inhomogeneous site density profile, 8
Insertion peptide, 230–231
Integral equation theory, 5
Interaction forces for linearized situations, 63–68
Interfacial tension, 32
Intermolecular correlation function, 3
Intermolecular interactions in lipid monolayers, 77–81
Intrinsic curvature, 2
Intrinsic partition coefficient, 243
Ion leakage in water pore formation, 128–129
Ionic charge imbalance in lipid membranes, 124–125
Ising model, xx
Isotherm slope, 91

Isotherms, 79, 81
    simulated and experimental, 91

Jablonski energy diagram, 190–191
Jump length, 211–212
Junctional proteins, 280

Killing domain in colicins, 228
Klenow fragment, 181

Lamellar lipid films and spin coating, 147–150
Lamellar phases in lipids, 43, 87
Landau theory, 86
Langmuir-Blodgett deposition technique, 83
Langmuir films, 77
Langmuir trough, 83–84
Laplace-Beltrami operator, 64
Laplace pressure, 82
Laser profiles, mathematical description of, 195–196
Laser scanning confocal microscopy (LSCM), 193–194
    limitations, 215–216
Laser trapping Raman spectroscopy for lipoprotein analysis, 276–278
Lateral compressibility of lipid monolayers, 79
Lateral diffusion coefficient, 79, 80
Lateral diffusion of lipids in membranes, 122–123
Lateral pressure in lipid monolayers, 89
Lateral pressure profiles, 30–32, 78
    affected by alcohols, 32–33
Lateral tension in supported lipid bilayers, 113–114
Lattice constant, 25–27
Lattice self-consistent field theory, 5
Leading-order approximations, 210
Leaflets in lipid bilayers, 108, 110–113
    flip-flops and, 129–130
Lemma of Ricci, 49
Lennard-Jones (LJ) potentials, 15, 86, 89–90, 107
Leukocidins, 231–232, 240
Linear stress-strain relation, 44
Lipid bilayers, 233–234
    coarse-grained models of, 2, 18–19
    composition of, 1
    fluids-DFT calculations of, 16–17
    mechanical properties of, 29–33
    multiscale modeling of supported, 101–115
    structure of, 17–29
Lipid composition in membrane, 242
Lipid density in bilayers, 17
Lipid flip-flops, 123–124
Lipid headgroups, 5
    centers of mass, 130–132
    and water pore formation, 126
Lipid headgroups in proteinaceous pores, 235
Lipid headgroups in supported lipid bilayers, 102
Lipid hydrocarbon tails, 5
Lipid interdigitation, 113
Lipid membranes
    collective dynamics in, 121–136
Lipid mixtures, model, 83
Lipid molecules, 76–77
Lipid monolayer tension-area isotherm, 90
Lipid monolayers, 75–97
    AFM of, 84–85
    applications of, 91–95
    in atomic detail, 91–92
    Brewster angle microscopy of, 84
    captive bubble surfactometer, 85
    compression of, 89
    computer simulations of, 86–95
    experimental studies of, 83–85
    fluorescence microscopy of, 84
    molecular density, 77–78, 85
    parameters affecting properties, 89–90
    phase behavior, 79–81
    properties, 76–83
    theoretical models of, 85–86
Lipid rafts, 244, 279
    model, 121
Lipid reservoirs, 82–83
Lipid self-assembly, 1
Lipid/solvent system and CMS-DFT, 11–12
Lipid structure, 22–24, 32–33
    affected by peptides, 25–29
Lipid tail entropy, 5
Lipid tilt field lines, 61
Lipid translocation across a membrane, 129–132
Lipidic pores, 236, 245
Lipoprotein lipase, 276
Lipoproteins, 285–286
    analysis of, 276–278
    and cardiovascular disease risk, 288
    life cycle of, 275–282
    magnetic resonance imaging of, 290–293
Liquid-condensed (LC) phase of lipid monolayers, 80–81, 91–95
Liquid-expanded (LE) phase of lipid monolayers, 79–81, 91–95
Liquid–liquid immiscibility, xvii–xxi
Liquid ordered state in membranes, 160
Low density lipoproteins (LDL) and cholesterol transport, 286–287
LSCM. *See* Laser scanning confocal microscopy (LSCM)
Lubricin, 265
Lung surfactant, 82–83
    modeling, 94–96

Macromolecules, detection of single, 173–180
Magainin, 236, 237
Magnetic resonance imaging, 290–293
Magnetically actuated tapping mode in atomic force microscopy, 156
MARTINI force field, 87, 90, 105–106, 109, 111
Mattress model of membrane-mediated interactions, 59
Mean-field approximation, 3
Mechanical equilibrium, 70
Mechanical properties affected by alcohols, 32–33
Mechanical signal transduction, 268–269
Mechanotransduction in cartilage, 266–268

MED-6215, 145
Membrane binding in pore formation, 246–247
Membrane elasticity, 43
Membrane insertion during pore formation, 247–248
Membrane-mediated interactions, 59–68
Membrane-membrane interactions and membrane support, 151–153
Membrane oligomers, 241
Membrane permeabilization, 249
Membrane-pore interface, 25–28
Membrane recognition by PFPs, 242–244
Membrane resealing, 132–133
Membrane shape, 58–59, 62–63, 66–68
Membrane stress tensor, 53–56
Membrane stresses and shape equilibria, 53–59
Membrane support and membrane-membrane interactions, 151–153
Membrane support materials, 144–146
Membrane surface potential, 243
Membrane tension, 44
Membranes, 216–217
    aqueous channels in, 223–249
    domains in, 159–160
    elastic properties of, 244
    electrostatic properties of, 243–244
    lipid composition, 242
    phase transitions in, 159–160
    thickness and aromatic belt, 244–245
Mesoscale modeling, 105–106, 109
Metric stress, 55
Metric tensor, 48
Mica as membrane support material, 144–145, 147, 152
Modified i-SAFT, 12–14, 22
Molecular density of lipid monolayers, 77–78, 85
Molecular dynamics, 102–103
    of lipid monolayers, 86–87
    simulations of lipid bilayers, 124
Molecular membrane theories, elements of, 3–6
Monocytes and triglyceride-rich lipoproteins (TGRLs) lipolysis products, 280–282
Monolayer collapse, 81–82
    simulation of, 94–96
Monolayer sliding in membrane bilayers, 46
Monte Carlo simulations, 4
Morphogenesis, 263
    cartilage, 264
Morphogens, 263–264
Multibody potential of mean force, 29
Multiscale modeling of lipid bilayers, 101–115

Nanopore analysis of nucleic acids, 171–184
Nanopore biosensors, 183
Net surface tension, 17
Neutral surface of membrane, 44
Nicolson approximation, 63
Noether's theorem, 54
Non-bilayer membrane, 236
Nucleation step in oligomerization, 248–249
Nucleic acid blockades, 173–180
Nucleic acids, nanopore analysis of, 171–184

Off-lattice self-consistent field theory, 5
Oligomerization, 224, 230–231, 249–250
    during pore formation, 248–249
Oligomers, 223
Orientational order parameter, 78
Osteoarthritis, 265, 268
Ostwald ripening, 163
Out-of-focus fluorescent noise, 193–194

Pair potential-based assembly energy, 28–29
Particle-based simulations, 2
Partition function, 3
Passive transmembrane transport of lipids, 123
Peptides affecting lipid structure, 25–29
Perfringolysin, 232
PFPs. *See* Pore-forming proteins (PFPs)
Phase behavior of lipid monolayers, 78–81
Phase coexistence region, 91
Phase diagrams in binary membranes, 161
Phase transition temperature, 79, 81, 89, 90, 92
Phase transitions in lipid monolayers, 86
Phase transitions in model membranes, 159–160
Phosphatidylcholine (PC), molecular structure of, 3–4
Phosphatidylserines, 4
Phospholipid films and spin coating, 147–148
Phospholipids complexing with cholesterol, xvii–xxi
Phosphorescence, 191
Photobleaching, 192, 201–202
    artifacts associated with, 216
    diffusion during, 215–216
    mathematical description of, 195–197
    stepwise, 240
Photon multiplier tubes, 194
Photons, 189
Planck's constant, 189
Plasma triglycerides, 275
Pneumolysin, 238–239
Poisson's ratio, 46–47
Polar angle, 235
Polar resides in proteinaceous pores, 235
Polyadenylic acid, 174–175
Polycytidylic acid, 175
Polyethylene glycol, 179
Polymer fluids and density functional theory, 7
Polymer-supported membranes, 145–146
POPC and spin coating, 147–148
Pore formation, 244–245
    influence of lipids on, 241–245
    and lipid flip-flop, 123–124
    mechanism of, 246–249
Pore-forming colicins, 228
Pore-forming peptides, 25–29
Pore-forming proteins (PFPs), 223–233, 236–341
    α-helix type, 224–230
    β-barrel type, 224, 227, 230–233
    determination of pores formed by, 236–237
    during pore formation, 246–249
    recognition of membrane, 242–244
Pore-forming toxins (PFTs), 224

Pore structures, 233–241, 245
    categories of, 234–236
    methods for determination, 236–241
Potassium chloride (KCl) in flip-flops, 132–133
Potential term, 57
Prefactor *k,* 50
Pressure tension in supported lipid bilayers, 113–114
Principal curvatures in membrane elasticity, 48
Principal directions in membrane elasticity, 48
PRISM theory, 10
Propagation step in oligomerization, 249
Propagator functions, 11–13
Protective antigen of anthrax toxin, 233
Protein–DNA interactions, 180–181
Protein interfacial concentration, 243
Protein-lined pore model, 234–235
Proteinaceous pores, 234–236, 245
Proteoglycans, 265
Protomers, 245
Proximal leaflet, 108, 110–113

Quantum numbers, 190
Quantum yield, 192

Radial distribution function, 3, 78
Raft hypothesis, 142
Random walk in membranes, 122
Receptor-binding domain in colicins, 228
Regions of interest (ROIs), 203–204
    size of, 216
Relaxivity in lipoprotein imaging, 291–293
Repulsive electrostatic interactions, 77–78
Reversible photobleaching, 216
Ribonuclease A, 180
Ricci tensor, 49, 70
Riemann tensor, 49, 50, 70
Rigid lipid models, 4–5
Rotational autocorrelation function, 79, 80
Rotational diffusion in lipid hydrocarbon chains, 122

Salt influence membrane interactions, 153
Saturated lipids of lungs, 82–83
Scalar energy density, 57
Scalar field of membranes, 56–57, 64–65
    in mediated interactions, 60–61
Scalars, 51, 52
Scale separation in biophysics, 41–43
Scanning force microscopy, 84
Scanning transmission electron microscopy (STEM), 239
Scavenger receptor class B type I (SR-BI), 287
Secondary fluorescence, 187
Segment density profiles, 12
Self-assembly of lipids, 4, 5
Self-consistent field (SCF) theory, 5
Shape equilibria and membrane stresses, 53–59
Shear strength of articular cartilage, 267–268
Shoulder-spike signature, 176
Signal transduction, mechanical, 268–269
Silcon, 104–105
Silicon oxide, 102
Silicon wafers as membrane support material, 145
Singlet electron state, 190–191
Site density of lipid bilayers, 21
Small unilamellar vesicles for supported lipid membranes, 143–144
Smectic liquid crystals, 159
Sodium chloride (NaCl) in flip-flops, 132–133
Solid condensed phase of lipid monolayers, 80–81
Solid-ordered state in membranes, 160
Spatial resolution in microscopy, 153, 158
Spherical micelles, 43
Spherical model fluids and density functional theory, 7
Sphingolipids, 76
Sphingomyelin, 242
Spin coating, 146–147, 169–170
    of lamellar lipid films, 147–150
Spin-coating precursor films, 150–151
Spinning-disc confocal microscope, 194
Splay modulus, 29
ssDNA-exonuclease I complexes, 180–181
Standard free energy in hairpin formation, 177
Staphylococcal α-hemolysin family, 231–232
State point, 16–17
Statins, 288
Statistical mechanical theory of molecular fluid, 3
Stepwise photobleaching, 240
Sterol lipids, 76
Sterols, 135
    and membrane recognition, 242
Stokes drag, 199
Stokes's Law, 191–192
Streptolysin O, 232, 249
Stress flux, 60–61
Stress profile across lipid membrane, 30–32
Stress-strain relation, 43–44
Stress tensor, 55–60
    in mediated interactions, 61–62
Stretching modulus, 44, 45
Superfacial zone protein (SZP), 265, 266, 268–269
Superposition principle, 63
Supported lipid bilayers, 101–115
    density profiles of, 107–108, 110–113
    materials for, 104–106
    mesoscale modeling of, 105–106, 109
    molecular simulations of, 102–104
    pressure and lateral tension in, 113–114
    visualizations of, 107–109
    water-free large-scale modeling of, 106–107, 109
Supported lipid membranes
    atomic force microscopy for imaging, 154–156
    fluorescence microscopy (FM) for imaging, 157–159
    by hydration of spin-coated precursor films, 150–151
    imaging microstrucure of, 153–154
    materials for, 144–146
    methods for preparing, 142–144
Surface free energy, 16–17
Surface granularity in lipid bilayers, 107
Surface Hamiltonians, 54, 55

Surface pressure-area isotherm, 79, 92–93
Surface pressure of lipid monolayers, 77, 81–82
Surface tension, 113–114
  of alveoli, 82
  of amphiphilic lipids, 77, 81
  of lipid monolayers, 81–82, 85, 87–91
  and membrane stresses, 54
Surface-tension coupling, 89
Surfactant-associated proteins B (SP-B), 82
Synoviocytes, 266

Tail beads in lipid bilayers, 21
Tailgroups, 5, 8, 15, 23–24, 31–32, 212
Tear film, 83
Temporal resolution in microscopy, 153–154, 156
Tensors, 48–49, 53–60, 70
Terminal base pair in nanopore analysis, 179
Ternary lipid mixtures, xviii–xix
Ternary model membranes, 162–164
Theorema Egregium, 50
Thermal energy in lipid membranes, 122
Thermal equilibrium, 70
Thermal fluctuations in flip-flops, 134–135
Thermodynamic consistent theories, 12
Thermotropic phases in membranes, 159–160
Three-dimensional pressure in lipid monolayers, 78
Time correlation functions, 79
Tip shape in atomic force microscopy, 156–157
Toroidal pores, 236
  morphology, 28
Total extrinsic curvature, 48, 51
Total internal refection fluorescence microscopy (TIRFM), 158–159
Toxins of staphylococcal α-hemolysin family, 231–232
Tramonto, 16
Transforming growth factor (TGF-β) superfamily, 264
  in chondrocytes, 258–269
Transient water probes in lipid membranes, 124–129
Translational ordering, 78
Translocation domain in colicins, 228
Transmembrane β-barrel, 230–231
Transmembrane domain in proteinaceous pores, 235
Transmembrane electric field in water pore formation, 125–126
Transmembrane ionic charge imbalance, 124–125
Transmembrane potential, 127–128
Traube's rule, 32
Triacylglycerol and chylomicrons, 286
Triglyceride-rich lipoproteins (TGRLs), 275–278
  and increased endothelial layer permeability, 280
  interaction with raft-like microenvironments, 280
  lipolysis products, 280–282
  products of, 279
Triplet electron state, 190–191
Tryalisin, 230
Tumor necrosis factor-alpha (TNFα), 276

Umbrella model of membrane insertion, 248
Undulation forces in membrane support, 152
Uniform laser beam, 200–201, 204
United atom type lipid model, 5–6
Unsaturated lipids of lungs, 82–83
Unzipping of hairpin molecules, 179

Vacuum/water interface in lipid monolayers, 87–90
van der Waals interactions, 77, 85
van der Waals potential, 151–152
Vector field, 57–58
  in mediated interactions, 61–62
  in membrane interactions, 65–66
Very-low-density lipoproteins (VLDLs), 279–281
Vesicle fusion for supported lipid membranes, 102, 143–144
Vesicle-to-bilayer transformation, 102
Vibrational relaxation, 191
Virial coefficients, 85

Wall potential and surface tension, 88–89
Water in supported lipid bilayers, 102
Water pore opening, 132–133
Water probe formation in lipid membranes, 124–129
Wave-particle duality of electromagnetic radiation, 188
Weeks-Chandler-Anderson potential, 107
Wertheim's first-order perturbation theory, 13
Wide-field fluorescence microscope, 193–194
Wilhelmy surface balance, 83
Wormhold model of pores, 236

X-ray crystallography for determining PFPs, 237–238

Young-Laplace law, 59
Young's modulus, 44, 45

Zero tension bilayer, density profiles, 17–18